University Library



A gateway to Melbourne's research publications

Minerva Access is the Institutional Repository of The University of Melbourne

Author/s:
Shi, S;Lam, N;Cui, Y;Lu, G;Gad, E;Zhang, L

Title:
Indentation modelling of aluminium cladding panels subjected to hailstone impact

Date:
2023-09

Citation:
Shi, S., Lam, N., Cui, Y., Lu, G., Gad, E. & Zhang, L. (2023). Indentation modelling of aluminium cladding panels subjected to hailstone impact. International Journal of Impact Engineering, 179, https://doi.org/10.1016/j.ijimpeng.2023.104638.

Persistent Link:
https://hdl.handle.net/11343/332562

Indentation modelling of aluminium cladding panels subjected to hailstone impact

Shuangmin Shi[a], Nelson Lam[a], Yiwen Cui[a], Guoxing Lu[b], Emad Gad[b], Lihai Zhang[a,*]

[a] Department of Infrastructure Engineering, The University of Melbourne, Parkville, VIC, 3010, Australia

[b] School of Engineering, Swinburne University of Technology, Hawthorn, VIC, 3122, Australia

Abstract

In spite of colossal damage caused to aluminium panels in hailstorms, there is currently no rational design procedure found on research to regulate the design of building claddings or rooftops to withstand hail impact. Damage predictive models that have been reported in the literature are not suited to predicting hail induced damage. Thus, insurance premiums on damage to aluminium cladding caused by hail cannot be set to fairly distribute risks. In the current study, an analytical model for predicting permanent indentation generated by the impact of a hailstone is presented. The model was developed from a combination of plate theories and results from thirty-seven full scale impact experiments conducted on 900 mm × 900 mm aluminium panels. The model presented in this article takes into account strain rate effects and has been demonstrated to give predictions that are within some 10% difference from experimental measurements.

Keywords: Permanent indentation; Aluminium cladding; Hailstone impact; Analytical model; Strain rate effect

*Corresponding author
E-mail addresses: shuangmins@student.unimelb.edu.au (S. Shi), ntkl@unimelb.edu.au (N. Lam), yiwcui1@student.unimelb.edu.au (Y. Cui), glu@swin.edu.au (G. Lu), egad@swin.edu.au (E. Gad), lihzhang@unimelb.edu.au (L. Zhang)

1. Introduction

A hailstorm event can inflict a considerable amount of damage to the cladding panels of a building. A cladding panel that has been impacted by hailstones may have its surface defaced requiring replacement. The replacement bills on damaged buildings in a city in the aftermath of a hailstorm can be up to tens of millions of dollars [1-3]. Should the storm intensity be severe enough to cause perforation of the panel allowing the ingress of water, colossal damage can be caused to the interior of the building and its contents [4, 5]. An accurate, and reliable, analytical method for predicting the extent of damage to cladding panels would serve the purpose of setting insurance premiums to fairly distribute risks, and providing realistic hazard assessments to guide decision making for optimising preventive measures.

Knowledge on damage prediction of impact actions is not commonly shared amongst building professionals. Realistic assessment of the risk of damage would need to involve resolving an impact action into two components: (1) global impulsive action and (2) localised contact action. The amount of deflection of a structural element caused by the impact of a heavy moving object is controlled by impulsive action. The prediction of the amount of deflection sustained by the element can be based on equal momentum and energy principles [6-9]. This analytical methodology, which is suited to dealing with the impact of a heavy moving impactor, gives more accurate predictions than the code stipulated equivalent quasi-static force method or the equal energy method [10]. However, the impact of a flying projectile, or a hailstone, on a cladding panel is more complex because of its highly transient and localised nature. With this type of impact scenario, the inflicted damage is more to do with the amount of force experienced at the point of contact on the surface of the panel (referred to herein as “contact force”). Quantification of contact force has been studied and reported [11-18]. Investigations into the impact resistance of different types of cladding products or metal panels such as roof sheeting [19], composite panels [20-24], and steel plates [25, 26], have also been reported in

47 the literature. However, no analytical predictive model for the impact by hail has been
48 developed. Thus, little is known of the amount of indentation that can be caused by hail impact
49 into an aluminium alloy panel which is a common type of installation in contemporary
50 buildings.

51 Sophisticated finite element (FE) software packages such as ABAQUS and LS-DYNA have
52 been used to simulate complex interactions between the ice specimen (the impactor) and the
53 surface of the test panel (the target) [27-29]. Advanced computational algorithms such as ALE,
54 and SPH, are claimed to be able to model the mechanical behaviour of the ice impactor [30-
55 33]. An important drawback with these simulation tools is that despite being validated by
56 experimental measurements, inconsistencies in their abilities to predict the same scenario have
57 been revealed among some of the published models [34]. Another important drawback of the
58 numerical simulation methodology in the context of day-to-day design practice is the high
59 demand for memory and computational time. The high computational cost is compounded by
60 the need for repetitive executions to achieve convergence. From the users' perspectives in the
61 context of day-to-day engineering practices, an experimentally validated analytical model is
62 much preferred to numerical (FE) models.

63 Plastic deformation of a metal plate has been studied extensively since the last century [35].
64 Investigations have been undertaken to predict irrecoverable transverse displacement when
65 subject to impulsive actions [36-39]. Membrane theory has been used to expedite the analysis
66 of a thin plate in response to an out of plane impact action [39-41]. Note, this type of analysis
67 is only valid if the amount of indentation relative to the thickness of the panel is large.
68 Analytical modelling for predicting permanent indentation into an aluminium alloy panel has
69 been treated in a few investigations [40-44]. Permanent indentation into the surface of an
70 aluminium panel was of interest in one of these studies [45]. However, the impact actions
71 considered in these cited references were not specific to hail impact which is unique in the

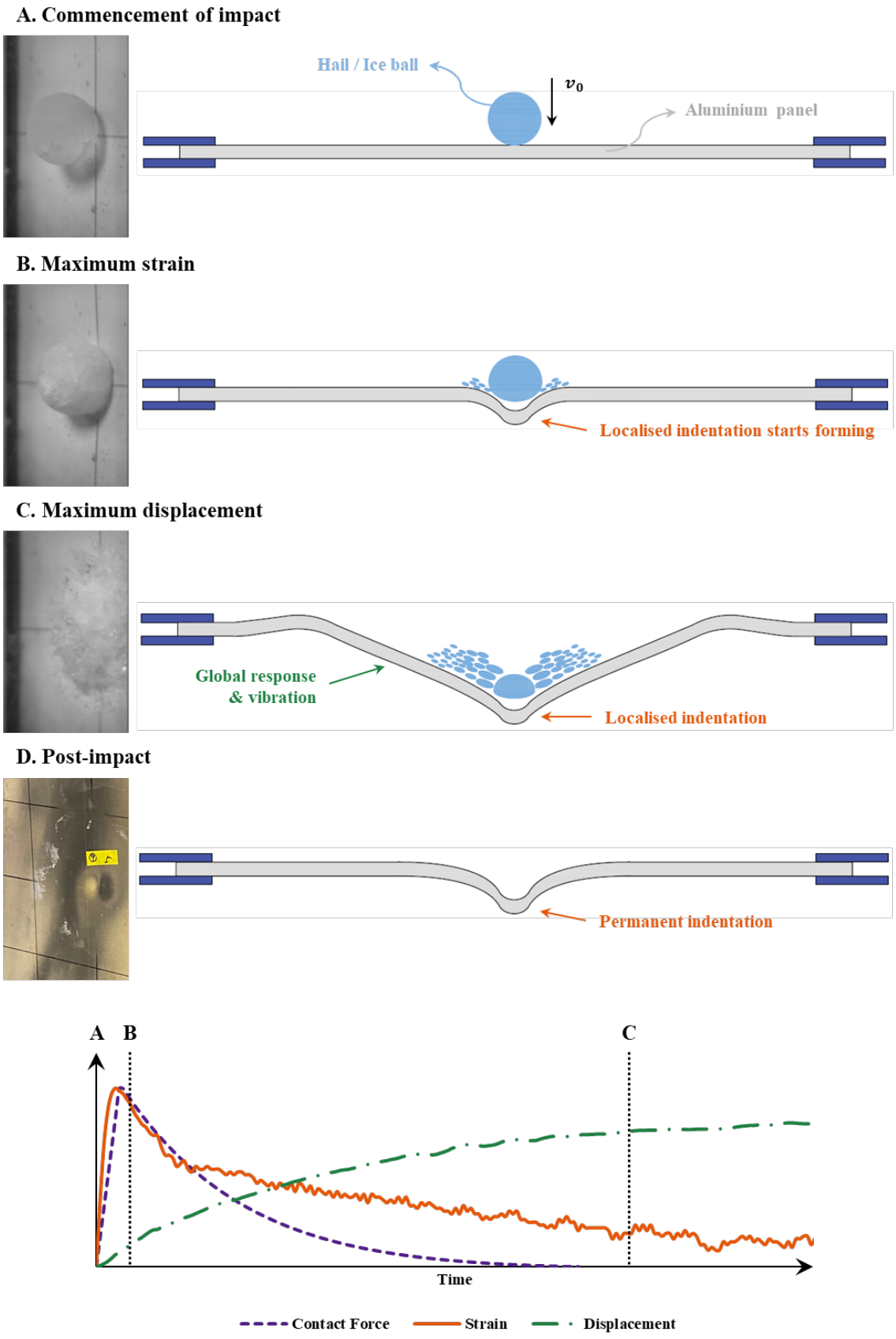
72 sense that the inflicted damage to the panel is very localised. With the impact by hailstones on
73 claddings, the amount of indentation can be small in comparison with the thickness of the
74 cladding in order that simplifications by membrane theory cannot be applied.

75 The original contribution of this study is the development of an analytical model for predicting
76 the amount of permanent indentation caused by hail impact into the surface of a (cladding)
77 panel made of aluminium alloy. Strain rate effects and contributions from both the membrane
78 and flexural actions have been incorporated in the derivation of the predictive expressions. The
79 schematic diagram of Fig. 1 shows different stages of a hail impacting an aluminium panel,
80 along with typical measurements of the contact force, strain, and displacement at the impact
81 point, as observed from impact experiments conducted in this study. Stage A is the time
82 instance when the ice impactor makes initial contact with the surface of the aluminium panel.
83 In less than half a millisecond, the magnitude of the contact force and the in-plane strain
84 increased monotonically with time prior to reaching the peak (Stage B). In experiments
85 conducted by the authors, cracks were observed to have propagated fully into the ice specimen
86 whilst localised indentation was formed in the aluminium panel. As the ice impactor
87 experienced disintegration and fragmentation, both the contact force and direct strain gradually
88 decreased back to zero. The global displacement of the plate, which took a much longer time
89 to react, eventually reached its fullest extent long afterwards (Stage C). The global response of
90 the plate which consisted mainly of elastic deflection and vibration eventually diminished
91 through energy dissipation by damping. In the end, permanent indentation was found at the
92 contact region (Stage D).

93 The accuracy of the proposed analytical model has been validated by comparison against
94 results from 37 impact tests conducted by the authors. Both the analytical and experimental
95 work presented in this article are original. To fulfil the stated project aim through impact

experimentation (the details of which are presented in Section 2), investigations were directed at the following topics:

I. Strain development time histories (Section 3.1) and strain rate effects (Section 3.2)
II. Indentation profile modelling (Section 3.3)
III. Permanent indentation estimates (Section 4.1)
IV. Experimental validation of the accuracy of model predictions (Section 4.2)
V. Example application of model (Section 5)



103

104 **Fig. 1. Schematic diagrams showing different stages of a hail impacting an aluminium panel and typical**
105 **measurements of contact force, strain and displacement at the impact point.**

2. Experimental Investigation

This section presents details of the testing program which involved the use of the gas gun accelerating ice impactors onto a specimen of the aluminium cladding. A total of 37 tests were performed and recorded, with the velocity of impact ranging from ~35 m/s to ~80 m/s. Observations and measurements from the full-scale impact experimentation provided valuable guidance in developing and validating the proposed damage prediction model, as presented schematically in Fig. 2.

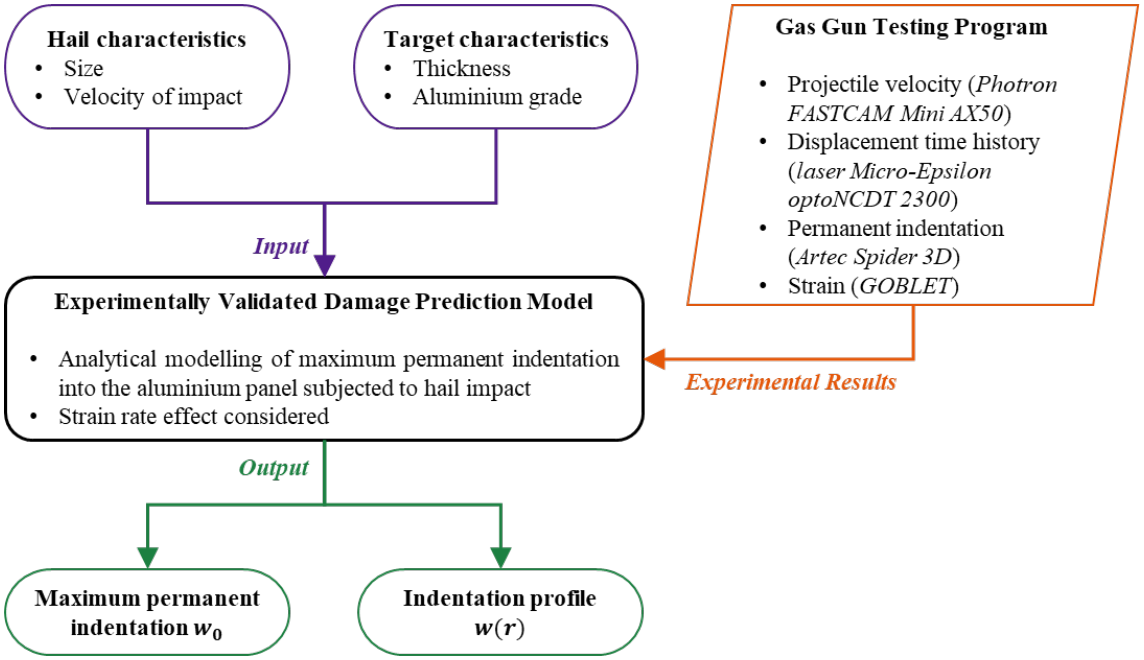
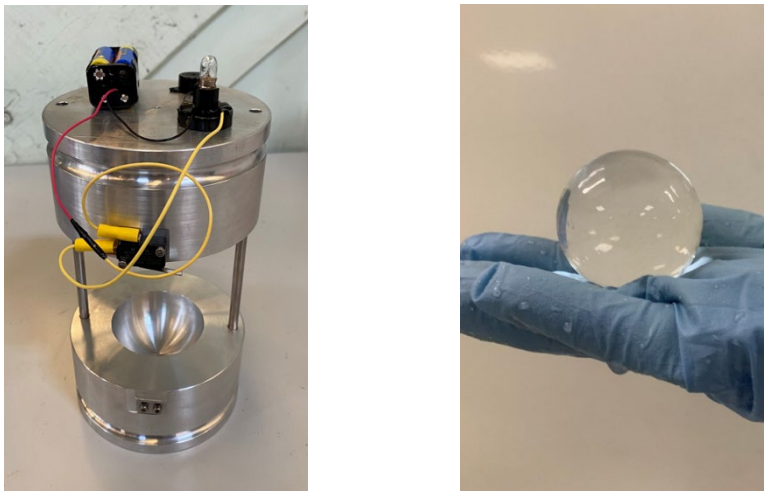


Fig. 2. A schematic overview of the framework of the developed analytical model in this study.

2.1. Spherical ice impactor

Spherical ice impactors with a diameter of 50.8 mm were fabricated for use in the impact tests. The size of these ice specimens was at the upper limit employed for impact testing of roofing panels for hail resistance according to relevant regulatory documents (ANSI/FM_4473 2011). To ensure that the specimens were free of cracks and air bubbles, vacuum-insulated cylindrical containers were used to facilitate top-down freezing [17, 18]. Ice cylinders frozen inside the

insulated containers were then melted using a custom-designed ice mould as shown in Fig. 3(a). The spherical mould was initially divided into two halves which were separated by the (slightly oversized) ice specimen. As the ice started to melt, the two halves of the mould came closer whilst forcing the ice into a sphere. A micro lever switch which was connected to a light bulb and an alarm was attached to the side of the mould to give signals to the user as soon as the two halves came in contact. This manner of moulding the ice specimen facilitates uniform cooling and avoids the formation of any air voids, or imperfections, as shown in Fig. 3(b). Testing with void-and-imperfection-free ice impactors has the benefit of making the experimental results repeatable in order to ensure a fair comparison with the deterministic model predictions.



(a) **(b)**

Fig. 3. Preparation of ice ball impactor: (a) a custom-designed ice mould for forming spherical ice specimen (b) a clear ice ball free of cracks for the impact test.

2.2. Aluminium alloy panel specimen

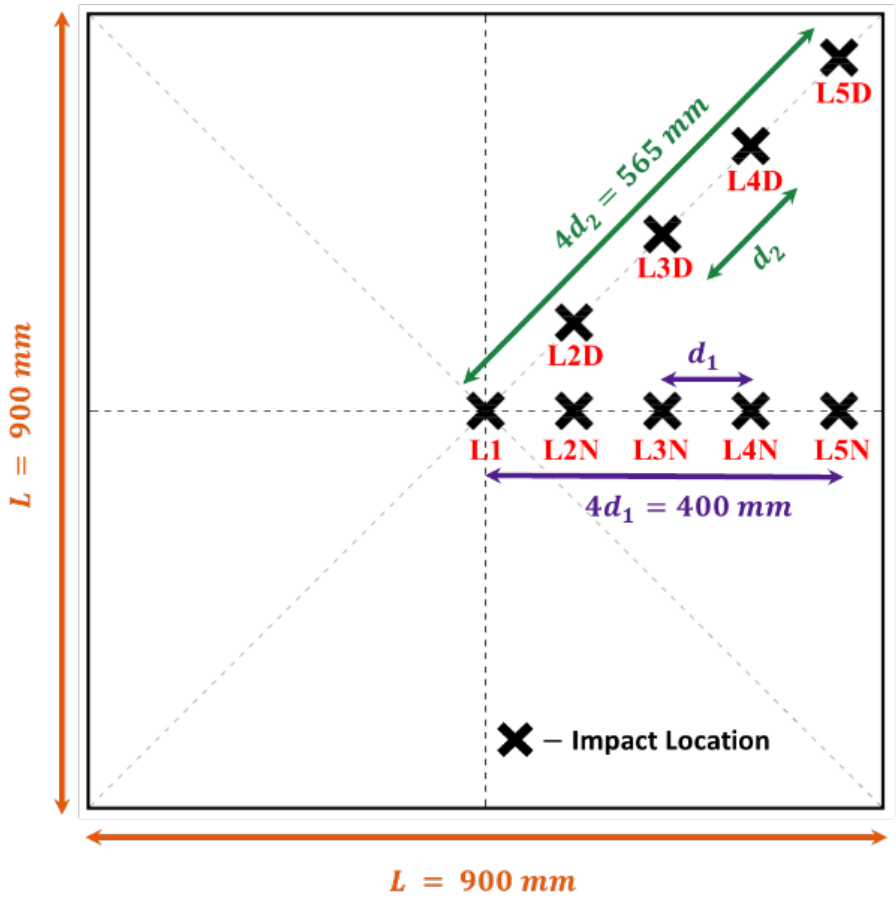
Aluminium panels (alloy 5083-H116) with planar dimensions of 1000 mm × 1000 mm and thicknesses of 3 mm and 4 mm were employed for the testing. The exposed area of the panel was 900 mm × 900 mm. Typically, cladding panels made of aluminium alloy with a thickness

of 3 mm or 4 mm are used in the global market. It is rare to see aluminium alloy cladding panels with larger thicknesses, except for sandwich panels which has a honeycomb structure as the core. Thinner panels are not recommended as they are prone to large deformations from intense impact by hailstones and windborne debris. Selection of the cladding panel specimen was guided by professional industrial advice [46] in which a standard panel with exposed dimension of 900 mm × 900 mm is specified. The analytical model presented in Section 4 has been validated by experimental results obtained from panels which are either 3 mm or 4 mm thick. By energy principles (as described in Section 4.1) the developed model is applicable to panels of different thicknesses.

In the impact tests, the panel specimen was struck at designated positions at 100 mm spacings along two straight lines in both the normal and diagonal directions as shown in Fig. 4(a). A photo taken from the panel specimen which was mounted on the test frame is shown in Fig. 4(b). The relevant material properties of the aluminium panels are listed in Table 1. The idea of having the test specimen impacted at multiple locations was to study the spatial variation of permanent indentation within the panel as commonly observed [46].

Table 1: Material properties of target aluminium panels samples with 3 mm and 4 mm thickness, respectively (ASTM B928M).

Alloy grade	Density (kg/m^3)	Elastic Modulus (GPa)	Yield Strength (MPa)	Dimensions (mm)
Aluminium 5083-H116	2660	71	215	900 × 900 × **3 (*THK*)** OR 900 × 900 × **4 (*THK*)**


L5D
L4D
L3D
L2D
$4d_2 = 565\ mm$
d_2
d_1
L1
L2N
L3N
L4N
L5N
$4d_1 = 400\ mm$
– Impact Location
$L = 900\ mm$
$L = 900\ mm$

159

160 **(a)**

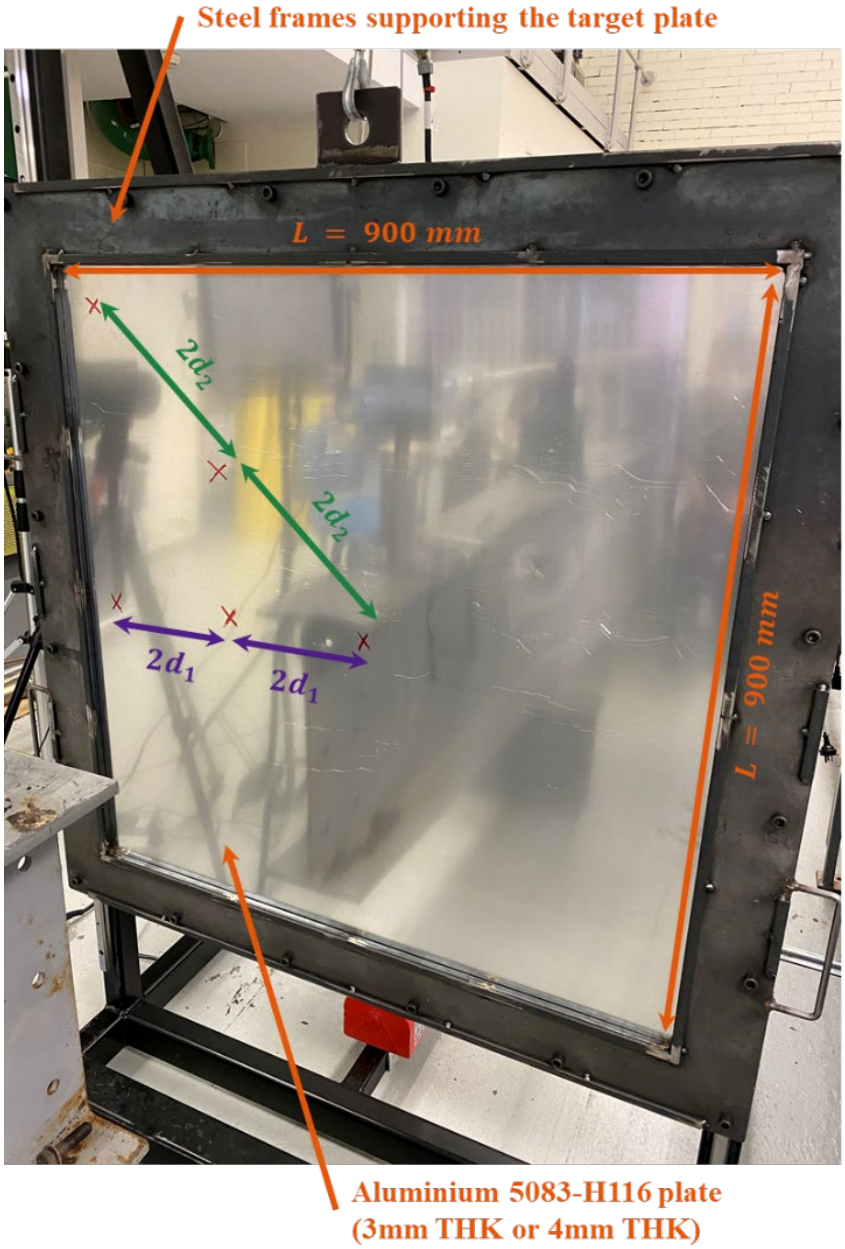


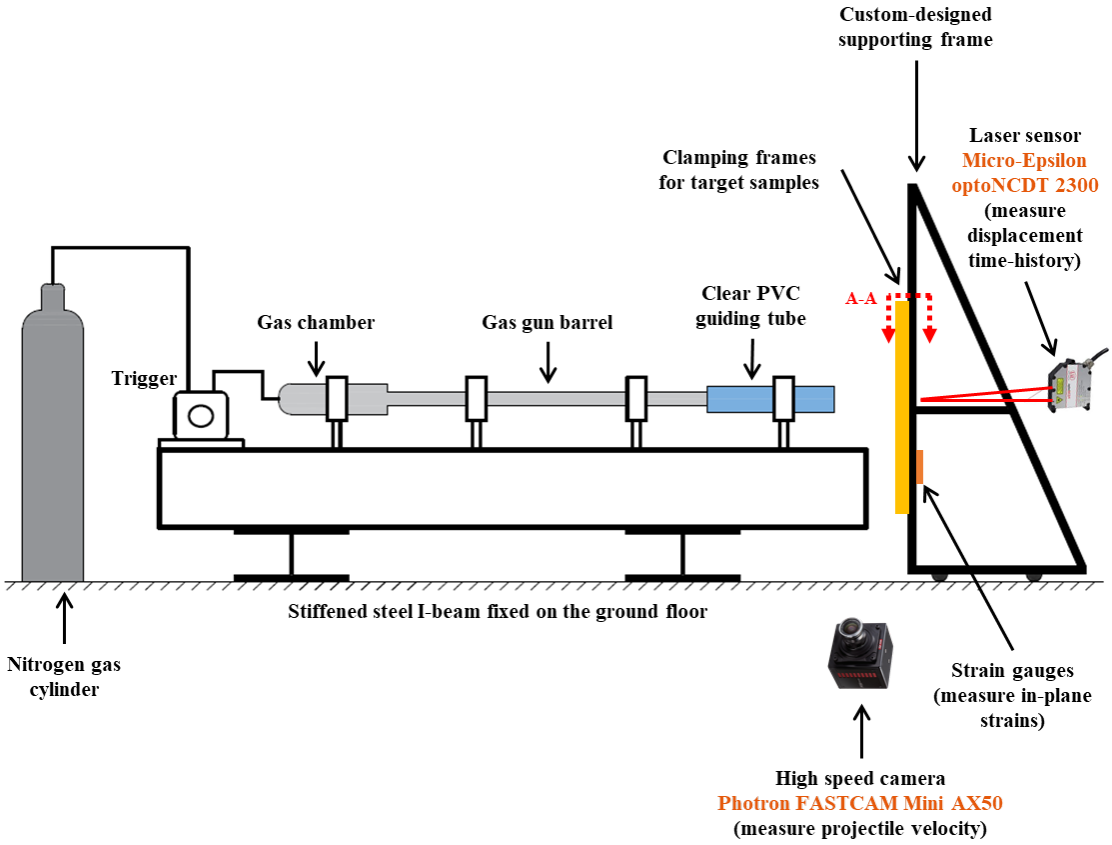
Fig. 4. (a) A schematic drawing of the panel specimen and locations of impact (b) a photo of one panel sample used in the impact test.

2.3. Setup of the gas gun testing

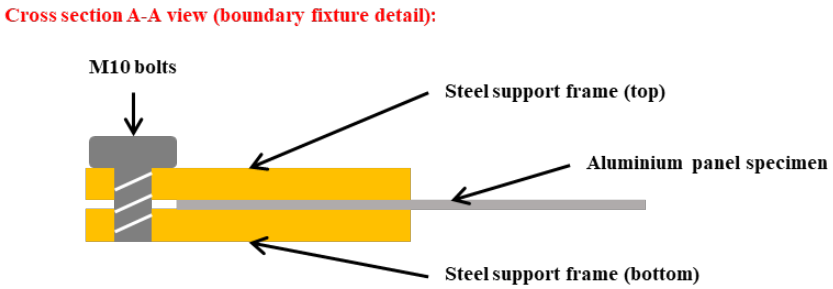
The experimental setup which is schematically shown in Fig. 5(a) features the use of compressed nitrogen gas for accelerating the ice impactor onto an aluminium panel which was supported by a custom-designed steel frame. The aluminium panel was sandwiched in between

two steel frames (10 mm in thickness) which were bolted together, representing a fully clamped boundary condition along the edges (Fig. 5(b)). The steel frame as shown in Fig. 6(a), was equipped with linear bearings and rails and an electric motor to give allowance for a full range of vertical movement. The black triangular stand, with wheels and sliding rails at the bottom, enabled the targeted panel to freely slide in the horizontal direction. The spherical ice impactor was launched through a steel gun barrel which was connected to a PVC guiding pipe to effectively minimise the melting of the ice specimen during launching. The incident velocity of impact of the ice projectile was measured using a high-speed camera (*Photron FASTCAM Mini AX50*) which was positioned in close proximity to the frontal surface of the targeted panel. The shooting angle was perpendicular to the direction of the projectile to improve measurement accuracy. The high-speed camera was set at 37,500 frames per second to capture images during the course of the impact. A laser sensor (*Micro-Epsilon optoNCDT-2300*) was also positioned at the rear side of the panel to record the displacement time history at the impact position. The laser sensor was securely fastened on the stationary steel I-beam and adjusted to align with the centreline of the gas gun barrel for a precise measurement at the impact position. Displacement signals were measured at a sampling frequency of 20 kHz over a measurement range of 300 mm. Multiple strain gauges were attached at both the front and back side of the panel specimen for measuring the in-plane strain time histories, as shown in Fig. 6(b) (these strain gauges had gauge factor of 2.13, resistance of 120 Ω and were connected to a *Wheatstone Bridge* with quarter-bridge configuration). The voltage signal from the bridge connection was first amplified and then recorded by an oscilloscope (*Tektronix TBS 2000B*) at a sampling frequency of 1 MHz. The triggering of the data acquisition was initiated by the laser sensor (edge trigger with a falling slope), and then synchronised with the high-speed camera and strain gauges to ensure consistency in the recorded timeframe. As the testing was completed, an optical 3D

scanner (*Artec Spider 3D*) was employed to measure the indentation profile of the damaged panel.

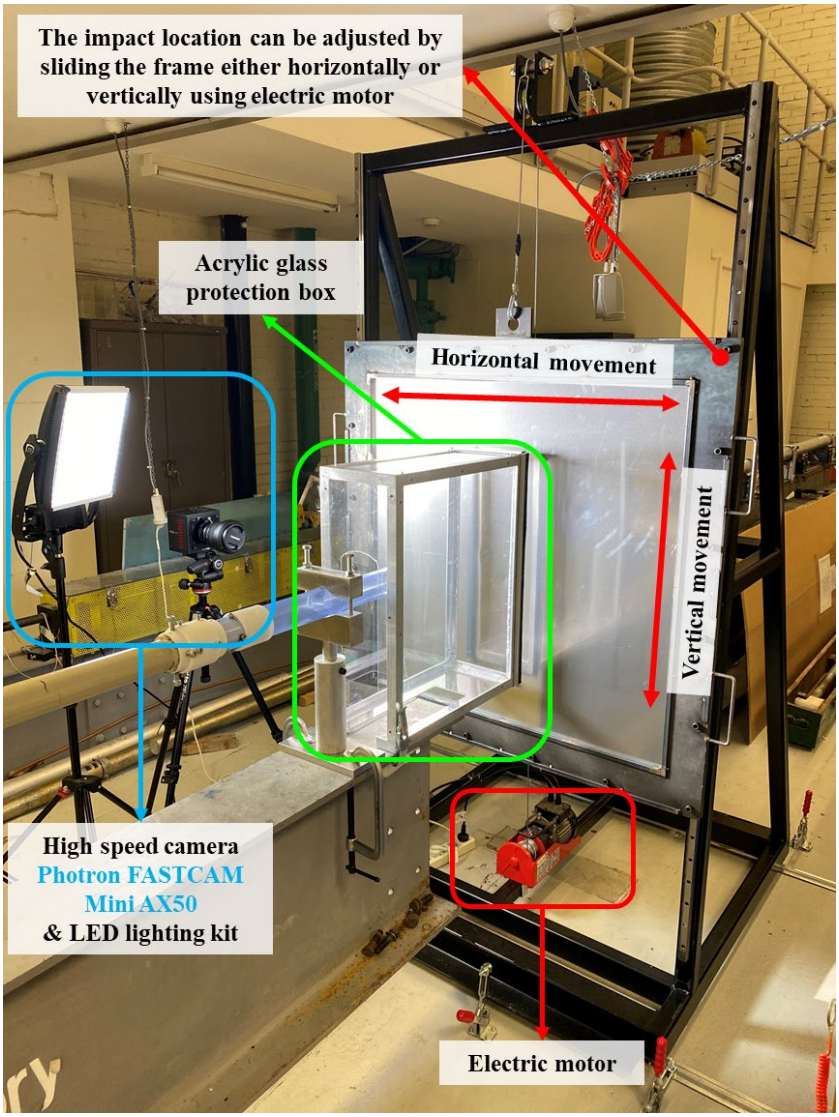


(a)

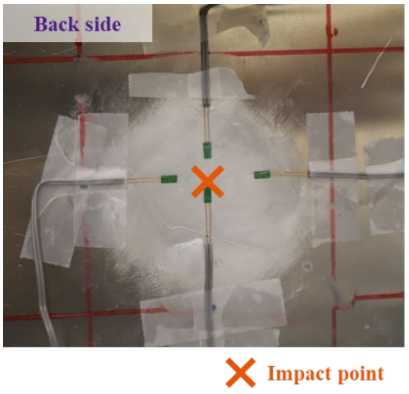


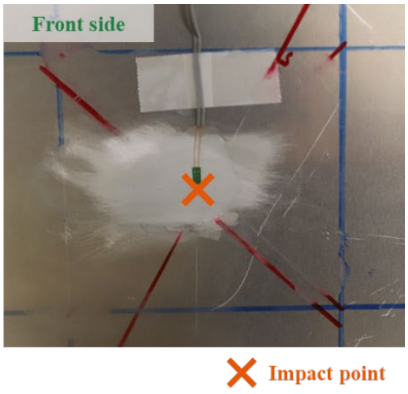
(b)

Fig. 5. (a) A schematic diagram of the experimental apparatus used in the impact test (b) zoom-in view of the boundary fixture details of the target panel.



(a)





(b) (c)

Fig. 6. (a) Photo of the experimental setup (b) photo showing the arrangement of strain gauges at the back side of the tested panel, strain gauges were attached with a distance of 0, 10, 15, and 20 mm away from the impact point (c) photo showing the arrangement of stain gauge at the front side of the tested panel, strain gauge was attached at the impact point.

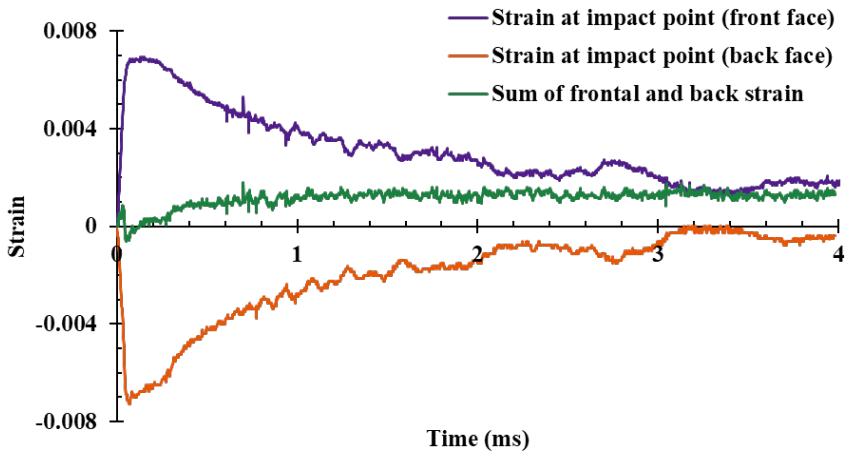
3. Testing Results

3.1. Strain time histories and timing of occurrence of permanent indentation

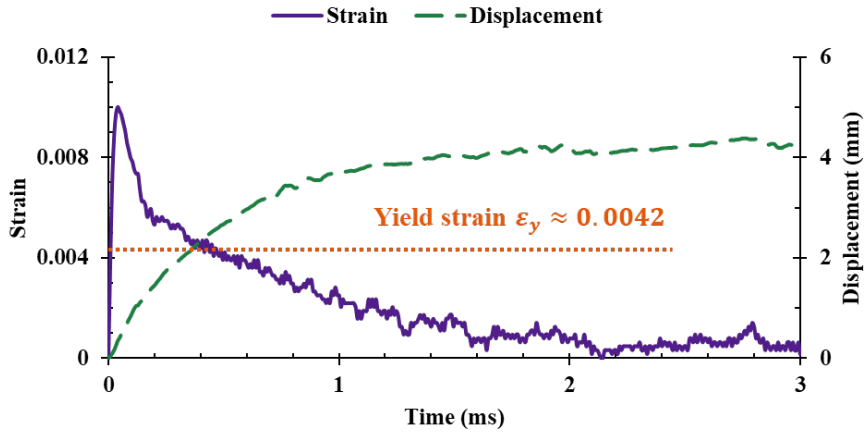
Strain gauges were attached to both sides of the panel to capture the rapid change in strains experienced by the specimen at the point of impact. Fig. 7(a) shows a typical record of the strain time histories which show that the surface strain at the front side of the panel (purple curve) was nearly symmetrical to that at the backside (orange curve). The summation of strains measured from both sides (green curve) was very small (~ 0) throughout the event, indicating that the neutral axis remained to be very close to the midplane of the plate implying little axial stresses. This observation has the important implication that the amount of membrane action was negligible (which was one of the assumptions made when developing the analytical model).

Overlaying the recorded displacement time history on the strain time history Fig. 7(b) reveals the timing of the formation of the permanent indentation. The occurrence of the peak strain (~ 0.1 ms) was considerably earlier than the occurrence of the maximum displacement (~ 3 ms) and is consistent with the behaviour as shown in the schematic diagrams of Fig. 1. For the impact scenarios considered in this study, the yield strain (ε_y) is approximately 0.0042 ($\varepsilon_y = \sigma_d/E = 297\ MPa/71\ GPa \approx 0.0042$; refer to Section 3.2 for more details), as shown by the annotation in Fig. 7(b). It can be inferred from the recorded time histories that irrecoverable indentation of the aluminium plate was fully formed in the first 1 ms, which was well before the deflection of the panel reaching its peak. It is also evident that there was no significant further increase in the amount of deformation after 1 ms, and no increase at all after 2 ms. The rapid fragmentation of ice upon impact has resulted in a rapid reduction in the stress concentration. As a result, the development of the localised stress and that of membrane action occurred at different times. Had the impactor been made of metal or other materials that would

remain intact during the collision, highly localised stress concentration would have lasted much longer thereby co-existing with membrane action in the vicinity of the impactor.



(a)



(b)

Fig. 7. (a) Experimentally measured strain time histories at the point of impact from the strain gauges attached at the front and the back side of the plate (b) experimentally measured strain and displacement time histories at the point of impact.

3.2. Mean strain rate and dynamic flow stress

The effect of strain rate should not be overlooked in the context of an impact scenario as considered in this study. Mean dynamic flow stress σ_d is introduced herein based on the

assumption of established flow relationships and Tresca yield criterion for rigid plastic material [47] which can be expressed in the form of the Cowper-Symonds equation as shown in Eq. (1).

$$\sigma_d = \sigma_y \left[1 + \left(\frac{\dot{\varepsilon_m}}{D}\right)^{\frac{1}{q}}\right] \quad (1)$$

where, σ_y is the yield stress of the aluminium alloy, $\dot{\varepsilon_m}$ is the mean strain rate, D and q are material constants which may be taken to be equal to 6700 and 4, respectively, for aluminium alloy [48].

All parameters in Eq. (1) are material constants except for the mean strain rate $\dot{\varepsilon_m}$, which can be measured experimentally. The value of the mean strain rate is taken as the average slope during the rise time which is defined herein as the period when the surface material strain increases monotonically from zero strain to peak strain. Fig. 8 shows the correlation between the mean strain rate and the ratio of the impact velocity (v_0) and plate thickness (t), in units of m/s and m, respectively. The experimentally measured mean strain rate was observed to be insensitive to changes in the size of the ice specimen which had diameter varying in the range: 31.8 mm ~ 50.8 mm, but was sensitive to variations in the value of v_0 and t ($\dot{\varepsilon_m}$ increases with increasing v_0, or decreasing t). The correlation is approximately linear when plotted to the logarithmic scale indicating a power law relationship; refer to Eq. (2).

$$\dot{\varepsilon_m} = 2.09 \left(\frac{v_0}{t}\right)^{0.45} \quad (2)$$

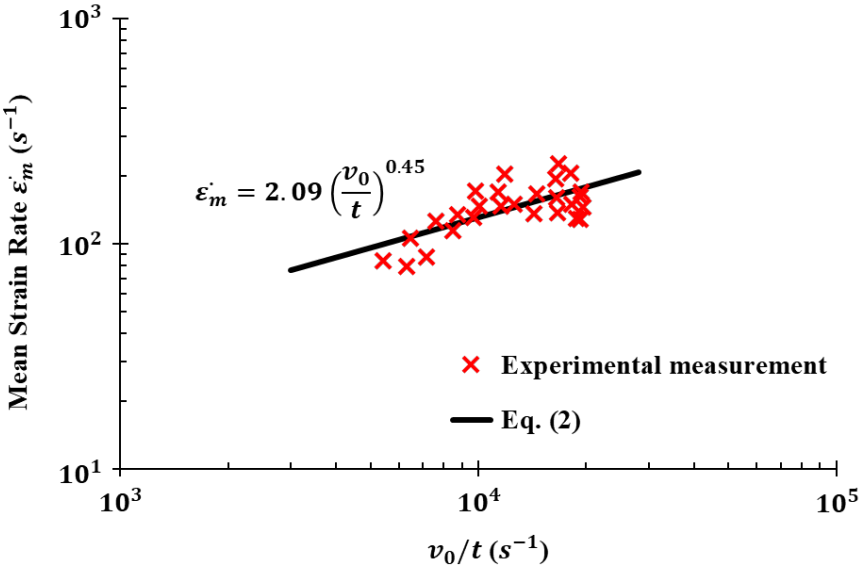


Fig. 8. Experimentally measured mean strain rate and its relationship with the velocity of impact and panel thickness. The spherical ice impactors had diameters of 31.8, 38.1, 44.5, and 50.8 mm.

Consider an imaginary impact scenario of an ice sphere impacting a 4 mm thick aluminium panel (5083-H116) at about 46 m/s. The mean strain rate as estimated from Eq. (2) is 140 s^{-1}. The dynamic flow stress according to Eq. (1) is calculated to be 297 MPa which is almost 1.4 times higher than the yield strength of the aluminium material (215 MPa). The significance of strain rate effects is evident.

3.3. Indentation profile

An optical 3D scanner (*Artec Spider 3D*) was used to scan the dented area on each tested (damaged) panel specimen following their impact testing. The scanned images were fused and reconstructed into 3D models via the *Artec Studio 15* and *Geomagic Control X* software. Fig. 9 shows some sample photos and scanned images of the permanent indentation. The presented contour maps were constructed by analysing the deformed surface with reference to a flat surface.

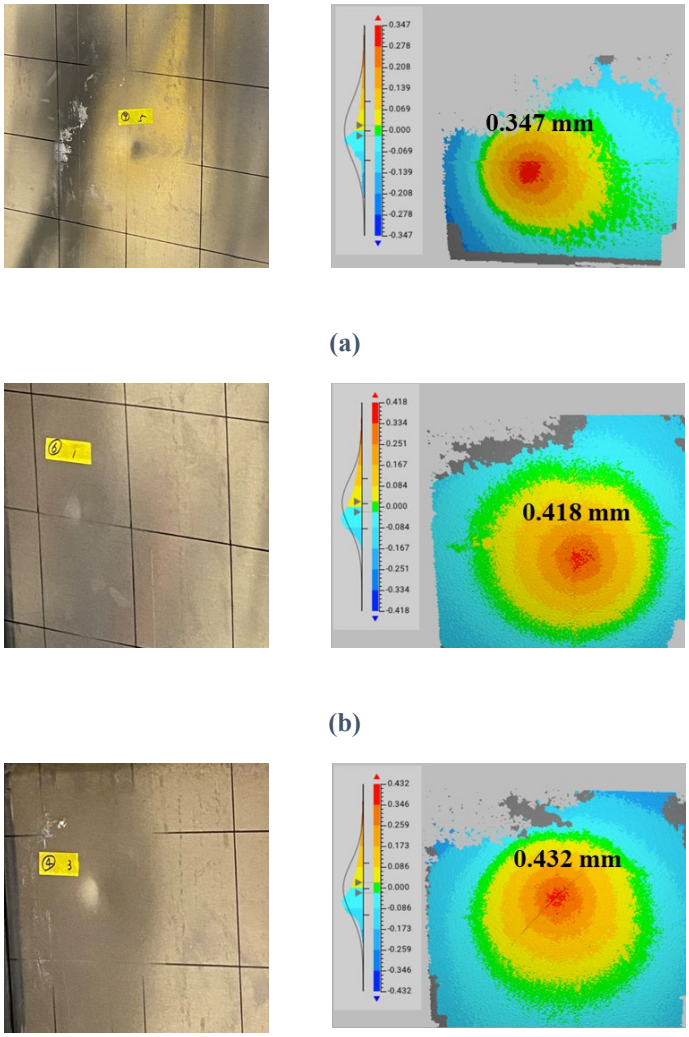


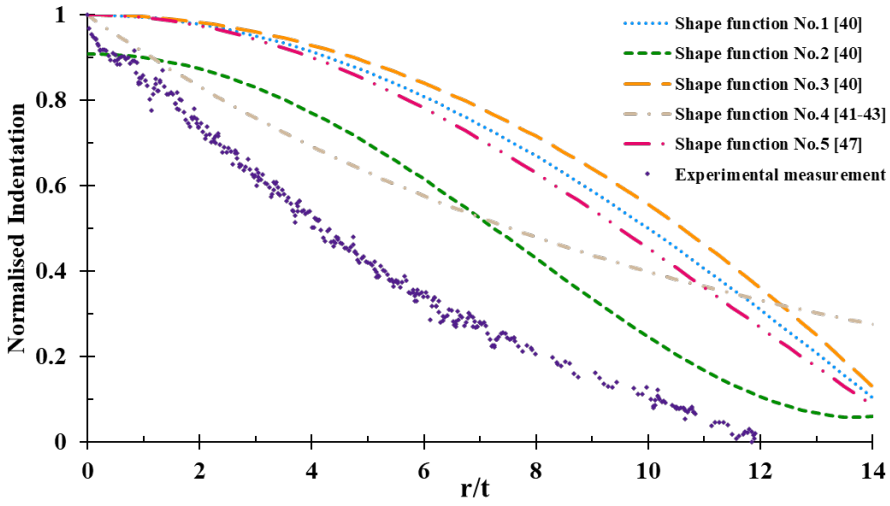
Fig. 9. Photos and scanned images of the permanent indentation (a) at location L1 (b) at location L5N (c) at location L5D.

Generalising the shape of indentation and having it expressed in the form of a mathematical relationship is the key to indentation modelling. A few assumed, and empirical curve fitted, deflection functions as reported in the literature are listed in Table 2. Note, these shape functions (as plotted in Fig. 10) were derived from studies of impact scenarios such as blast or collision by a large mass. The deflections of the panel in those scenarios are dominated by global plastic deformation. Thus, the shape of the indentation of the panel in a hail impact scenario might not be represented accurately by any of the listed shape functions.

295 **Table 2: Assumed or empirically fitted deflection shape reported in the literature.**

No.	Shape function	Comments
1.	$w(r) = w_0 \cos\left(\frac{\pi r}{2R}\right)$	[40]
2.	$w(r) = w_0\left[0.909 - 2.03\left(\frac{r}{R}\right)^2 + 1.21\left(\frac{r}{R}\right)^4\right]$	[40]
3.	$w(r) = w_0\left[1 - \left(\frac{r}{R}\right)^2\right]$	[40]
4.	$w(r) = w_0 e^{-0.023r}$	[41-43]
5.	$w(r) = w_0 J_0\left(\frac{a \cdot r}{R}\right)$	[47]

296



297

298 **Fig. 10. Comparisons of the shape functions reported in the literature with experimental measurements.**

299

300 Eq. (3) is proposed herein to generalise the normalised indentation profile of hail impact.
301 Coefficients in the expression were found by calibration against experimental observations.

302 $$w(r) = w_0 e^{-b\cdot(r/t)^a} \quad (3)$$

303 where, $w(r)$ is the normalised profile of the permanent indentation, w_0 is the maximum
304 amount of permanent indentation occurring at the impact point, r is the radial distance

measured from the point of impact, t is the thickness of the aluminium panel, and a and b are coefficients the values of which can be obtained by calibration against empirical (experimental) data.

Further analysis of the experimentally measured indentation profile was undertaken by extracting the 3D data cloud points to reconstruct the cross-sectional profile at the point of impact; refer to Fig. 11. Specific details associated with the eleven sets of experimental data used for calibrating the coefficients: a and b of Eq. (3) are listed in Table 3. Although the location of the point of contact associated with each indentation profile varies between the data sets, negligible differences can be seen in their shapes. The calibrated values for parameters a and b, as derived using the Curve Fitting Toolbox in MATLAB, are 1.4 and -0.09, respectively. Eq. (3) is accordingly rewritten as Eq. (4).

$$w(r) = w_0 e^{-0.09(r/t)^{1.4}} \quad (4)$$

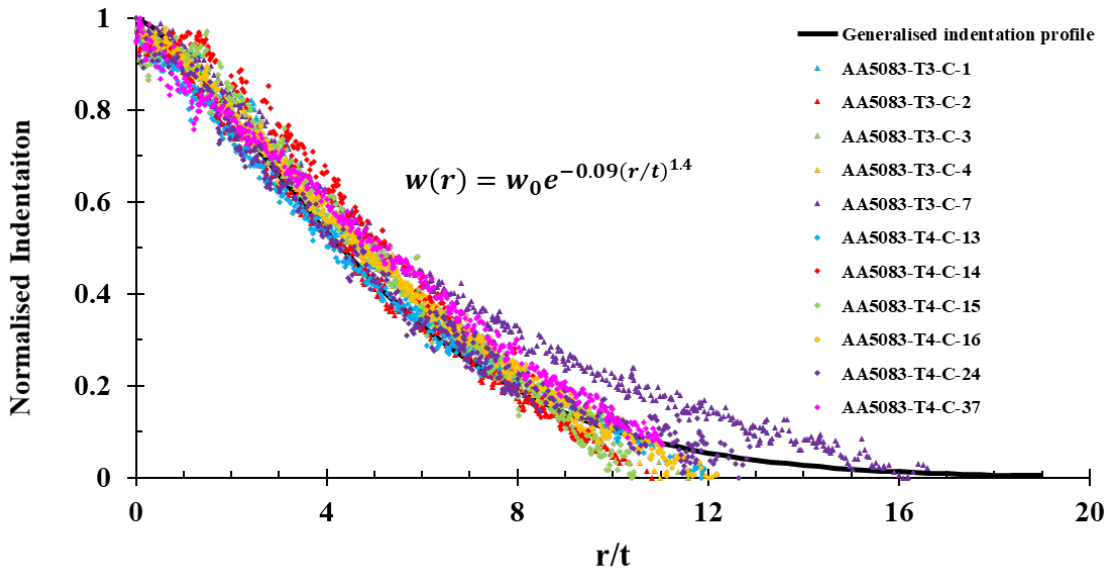
As the position of impact was varied the normalised indentation profile across the data sets were found to be highly consistent. The diameters of the permanently dented area of the tested specimens was found to be within 100 mm, revealing the localised nature of the permanent indentation. Thus, Eqs. (3) and (4) are generally applicable to panels of different sizes.

Table 3: 11 sets of experimental data used for studying the indentation profile.

Test ID	Impact velocity (m/s)	Panel thickness (mm)	Impact location	w_0 (mm)
AA5083-T3-C-1	46.88	3	L1	0.480
AA5083-T3-C-2	51.49	3	L2N	0.608
AA5083-T3-C-3	50.35	3	L2D	0.598
AA5083-T3-C-4	54.46	3	L3N	0.664
AA5083-T3-C-7	44.45	3	L3D	0.483
AA5083-T4-C-13	78.25	4	L1	0.451
AA5083-T4-C-14	73.09	4	L2N	0.375
AA5083-T4-C-15	76.92	4	L2D	0.391

AA5083-T4-C-16	77.30	4	L3N	0.466
AA5083-T4-C-24	64.33	4	L4N	0.283
AA5083-T4-C-37	79.10	4	L5D	0.525

322



323

324 **Fig. 11. Normalised indentation profile measured experimentally and estimated from empirical equation**
325 **Eq. (4).**

4. Analytical Model Development

This section presents the conception and development of an analytical model for predicting the maximum permanent indentation into an aluminium cladding panel induced by hail impact. Section 4.1 demonstrates the fundamentals of quantifying the amount of energy expended in plastic straining for a given amount of (initial) kinetic energy delivered by the impact. The derivation and validation of the algebraic predictive relationship are presented in Section 4.2, along with an extra note in Section 4.3.

4.1. Energy expended in plastic straining

The total amount of energy expended in plastic straining causing permanent indentation into the metal (W_p), referred to herein as "plastic work", can be expressed as the volume integral of the sum of the product of radial and circumferential stresses and their respective strains as presented in Eq. (5). The equality was derived from thin plate theory and was based on the assumption of plane stress and symmetric conditions (i.e., the *Kirchhoff* assumption). The stated assumptions can be justified by reference to the experimental observations as presented in Section 3.1.

$$W_p = \int_{vol}[\int(\sigma_r d\varepsilon_r + \sigma_\theta d\varepsilon_\theta)]\, dV \tag{5}$$

where, W_p is the plastic work, and σ_r, σ_θ, ε_r, and ε_θ are the stresses and strains in the radial and circumferential directions, respectively.

The relevant strains can be found using Eqs. (6b) and (6b) below.

$$\varepsilon_r = \varepsilon_m + \varepsilon_{rb} = \frac{1}{2}\left(\frac{\partial w}{\partial r}\right)^2 + z\kappa_r \tag{6a}$$

$$\varepsilon_\theta = \varepsilon_{\theta b} = z\kappa_\theta \tag{6b}$$

where, ε_m , ε_{rb} , and $\varepsilon_{\theta b}$ are the radial membrane strain, radial bending strain, and circumferential bending strains respectively; z represents the direction of indentation (transverse) in a cylindrical coordinate system as depicted in Fig. 12; κ_r and κ_θ are the radial and circumferential curvatures as expressed in Eqs. (7a) and (7b).

$$\kappa_r = -\frac{\partial^2 w}{\partial r^2} \tag{7a}$$

$$\kappa_\theta = -\frac{1}{r}\frac{\partial w}{\partial r} \tag{7b}$$

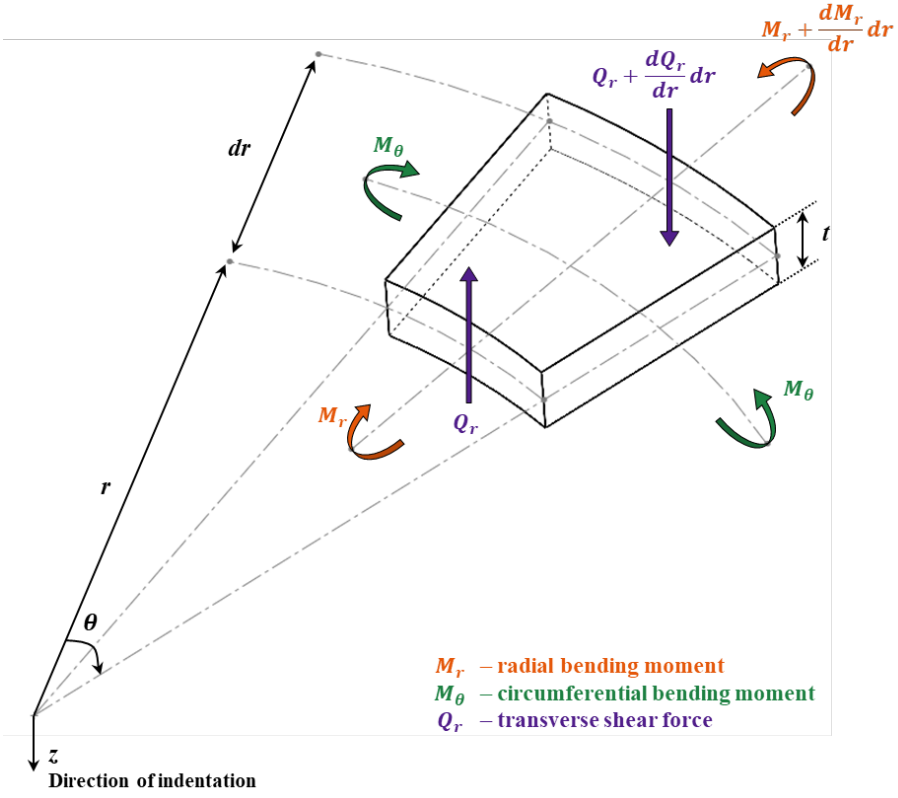


Fig. 12. Cylindrical coordinate system and notation used in this study.

The magnitude of various stresses that are developed in the radial and circumferential directions can be found using the presented relationships along with Eq. (1) which provides an estimate for the mean dynamic flow stress σ_d. The total amount of plastic work can be found

359 by the substitution of Eqs. (1), (6) – (7) into Eq. (5). The result of the substitution can be
360 expressed in the form of Eq. (8).

361 $$W_p = W_m + W_{rb} + W_{\theta b} = \int_{vol} \sigma_d(\varepsilon_m + \varepsilon_{rb} + \varepsilon_{\theta b})\, dV \quad (8)$$

362 where, W_m, W_{rb}, and $W_{\theta b}$ are the plastic work components attributed to the radial membrane
363 force (stress), radial bending moments, and circumferential bending moments, respectively.
364 The full expressions for all three plastic work terms are shown in Eqs. (9a) – (9c).

365 $$W_m = \pi\sigma_d t \int_0^R \left(\frac{\partial w}{\partial r}\right)^2 r\, dr \quad (9a)$$

366 $$W_{rb} = \frac{1}{2}\pi\sigma_d t^2 \int_0^R \left(-\frac{\partial^2 w}{\partial r^2} r\right) dr \quad (9b)$$

367 $$W_{\theta b} = \frac{1}{2}\pi\sigma_d t^2 \int_0^R \left(-\frac{\partial w}{\partial r}\right) dr \quad (9c)$$

368 where, R is the radial distance measured from the point of impact to the edge of the dented area,
369 and w is the indentation profile as defined by Eq. (4).

370 Substituting Eq. (4) into Eqs. (9a) – (9c) gives Eqs. (10a) – (10c) for quantifying the respective
371 components of the plastic work. Note that γ represents the lower incomplete gamma function.

372 $$W_m = \frac{7}{20}\pi\sigma_d t w_0^2 \left\{1 - \gamma\left[2, 0.18\left(\frac{R}{t}\right)^{1.4}\right]\right\} \quad (10a)$$

373 $$W_{rb} = \frac{1}{2}\pi\sigma_d t^2 w_0 \left\{1.4\gamma\left[2, 0.09\left(\frac{R}{t}\right)^{1.4}\right] - 0.4\exp\left[-0.09\left(\frac{R}{t}\right)^{1.4}\right] - 1\right\} \quad (10b)$$

374 $$W_{\theta b} = \frac{1}{2}\pi\sigma_d t^2 w_0 \left\{1 - \exp\left[-0.09\left(\frac{R}{t}\right)^{1.4}\right]\right\} \quad (10c)$$

375 Fig. 13 shows the percentage contribution to the total plastic work (W_p) by each of the three
376 components (W_m, W_{rb}, and $W_{\theta b}$), as found using Eqs. (10a) – (10c). The presented results were
377 derived from a diversity of impact scenarios as characterised by the indentation-to-thickness

ratio (w_0/t). It is shown that the amount of plastic work done by the radial and circumferential bending moments were the main contributors to energy absorption by the aluminium panel. As the intensity of impact was increased (i.e., when w_0/t became higher) the amount of contribution from the radial membrane forces (and stresses) was increased. Contributions by bending were reduced. It is noted that in a hail impact scenario, the level of intensity is generally small. The amount of indentation is typically less than the thickness of the panel, as shown in Table 3. In summary, the assumption of neutral midplane and the application of plate bending theory is generally valid for dealing with the impact action of hail. Should there be a situation where the amount of indentation exceeds the panel thickness ($w_0/t > 1$), the amount of plastic work done which is attributed to membrane action can become the dominant source of energy dissipation, as reported in the literature [49, 50].

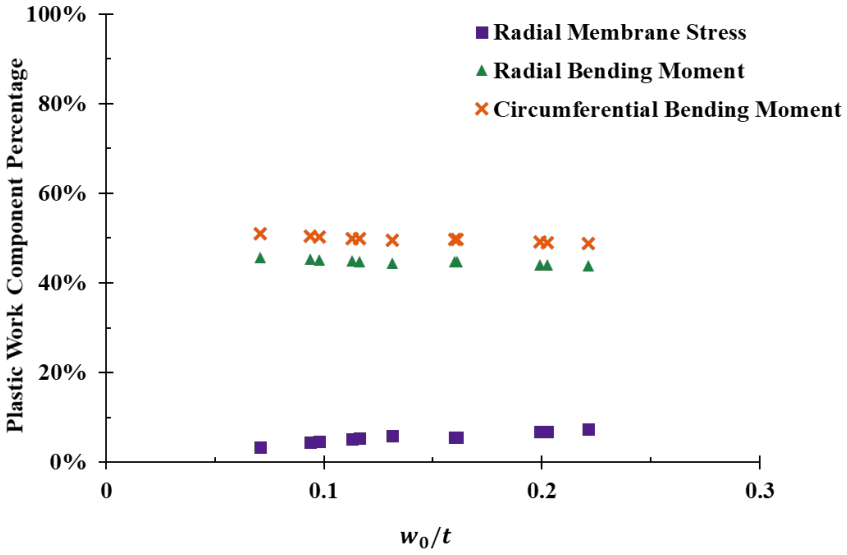


Fig. 13. Comparison of the plastic work component done by radial membrane stress, radial bending moment, and circumferential bending moment in different impact scenarios.

Table 4 summarises the total amount of plastic work consumed in each of the tested scenarios as calculated using Eqs. (8), (10a) – (10c), and the amount of kinetic energy delivered by the impact, as shown in Table 3. The plastic work to kinetic energy ratios are also listed.

396 **Table 4: Summary of the total plastic work, initial kinetic energy, and plastic work to kinetic energy ratio.**
397

Test ID	Total plastic work W_p (J)	Initial kinetic energy KE_0 (J)	$\frac{W_p}{KE_0}$
AA5083-T3-C-1	4.02	64.84	6.21%
AA5083-T3-C-2	5.17	78.22	6.61%
AA5083-T3-C-3	5.08	76.06	6.68%
AA5083-T3-C-4	5.68	88.96	6.38%
AA5083-T3-C-7	4.06	59.27	6.85%
		Average	**6.55%**
AA5083-T4-C-13	3.83	180.62	2.12%
AA5083-T4-C-14	3.15	157.59	2.00%
AA5083-T4-C-15	3.29	174.56	1.89%
AA5083-T4-C-16	3.95	176.27	2.24%
AA5083-T4-C-24	2.35	122.09	1.93%
AA5083-T4-C-37	4.49	187.68	2.39%
		Average	**2.09%**

398

399 The plastic work and initial kinetic energy values as recorded from the impact experiments (as
400 listed in Table 4) can be summarised into Eqs. (11a) and (11b).

401 $$\left.\frac{W_p}{KE_0}\right|_{t=3\ mm} \approx 6.55\% \qquad \text{for a plate with a thickness of 3 mm} \qquad (11a)$$

402 $$\left.\frac{W_p}{KE_0}\right|_{t=4\ mm} \approx 2.09\% \qquad \text{for a plate with a thickness of 4 mm} \qquad (11b)$$

403 The value of W_p may be estimated conveniently using Eqs. (11a) and (11b) for impact
404 scenarios where the initial kinetic energy (mass-velocity combination) delivered by the
405 impactor is known.

406 ### 4.2. An algebraic expression for determining the permanent indentation

407 Substituting Eqs. (10a) – (10c) into Eq. (8) and rearranging the terms gives Eq. (12) which
408 provides predictions for the value of w_0.

409 $$w_0 = \frac{1}{2}\left(-t\frac{\mathrm{B}}{\mathrm{A}} + \sqrt{t^2\frac{\mathrm{B}^2}{\mathrm{A}^2} + \frac{4W_p}{\pi\sigma_d t\mathrm{A}}}\right)$$

410 - $$\mathrm{A} = 0.35\left\{1 - \gamma\left[2, 0.18\left(\frac{R}{t}\right)^{1.4}\right]\right\}$$

411 - $$\mathrm{B} = \left\{1 - 0.3\exp\left[-0.09\left(\frac{R}{t}\right)^{1.4}\right] - 0.7\gamma\left[2, 0.09\left(\frac{R}{t}\right)^{1.4}\right]\right\} \quad (12)$$

412 Note, the value of R may be treated as a constant, and is taken as 50 mm, which is the maximum
413 radius of the dented area on the aluminium panel as observed from the experiments conducted
414 by the authors. Coefficients A and B are also constants for a given thickness (t) of the panel.
415 These values of the coefficients for two common panel thicknesses are listed in Table 5.

416 **Table 5: Numerical values of A and B for panels with a thickness of 3 mm and 4 mm.**

Aluminium panel thickness (mm)	A	B
3	0.3499	0.9422
4	0.3454	0.7743

417

418 In summary, the amount of permanent indentation into the aluminium plate (w_0) can be
419 predicted with the combined use of Eqs. (1), (2), (11a) or (11b), and (12), when the size (mass)
420 of the hail, the velocity of impact, the thickness and grade of the target aluminium panels are
421 well defined. The accuracy of the proposed analytical expression (Eq. (12)) has been validated
422 by comparisons against an additional twenty-six sets of experimentally measured permanent
423 indentations that are different to the results listed in Table 3 (that were employed in the
424 calibration of the coefficients). Thus, the experimental results involved in the comparison are
425 therefore independent of the calibration process. Comparisons of the predictions against these
426 independent measurements are presented in Fig. 14 for impact scenarios across different panel
427 thicknesses and impact velocities. Numerical discrepancies between the predicted results from

Eq. (12) and experimental measurements were all within 10%. The outcome of the comparison assures the accuracy of the proposed hand calculation procedure.

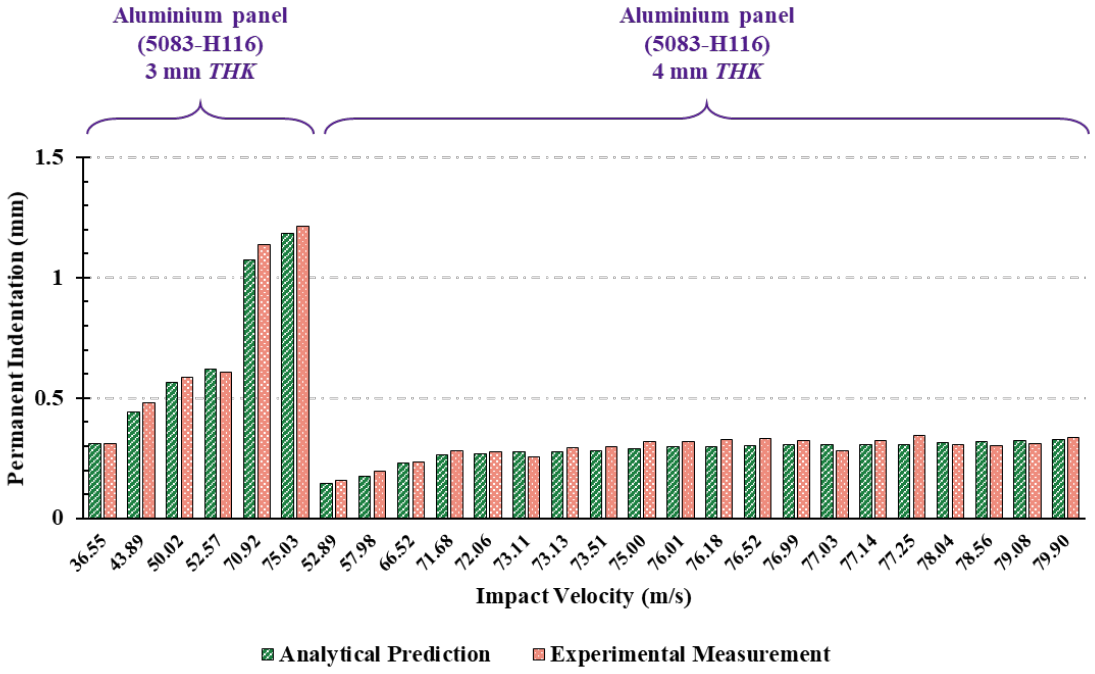


Fig. 14. Comparison of permanent indentations predicted by the analytical expression and experimentally measured by the optical 3D scanner.

4.3. A note on the spatial variance of indentation

In an earlier investigation employing metal impactors, the amount of permanent indentation into the aluminium panel was reported to be increasing with decreasing distance between the impact position and the closest supporting edge of the panel [44, 51]. Interestingly, this spatial variation was not observed in the current study which deals with hail impact. The reason is that the amount of permanent indentation generated by the impact of ice was too small to be captured. Fig. 15 shows comparisons of some experimentally measured permanent indentations against different locations of impact when the impact velocity was kept unchanged. There is a weak trend showing the amount of indentation to increase slightly impact position moves closer to the supporting edge of the panel. However, the observed variation was too minor to warrant

it incorporated into the analytical model. The amount of variation is also controlled by the yield strength of the alloy. The 5083-H116 (215 MPa) alloy adopted in this study is believed to have suppressed the spatial variation because of its higher yield strength in comparison with other alloy grades such as 5005-H34 (105 MPa) and 5052-H32 (160 MPa).

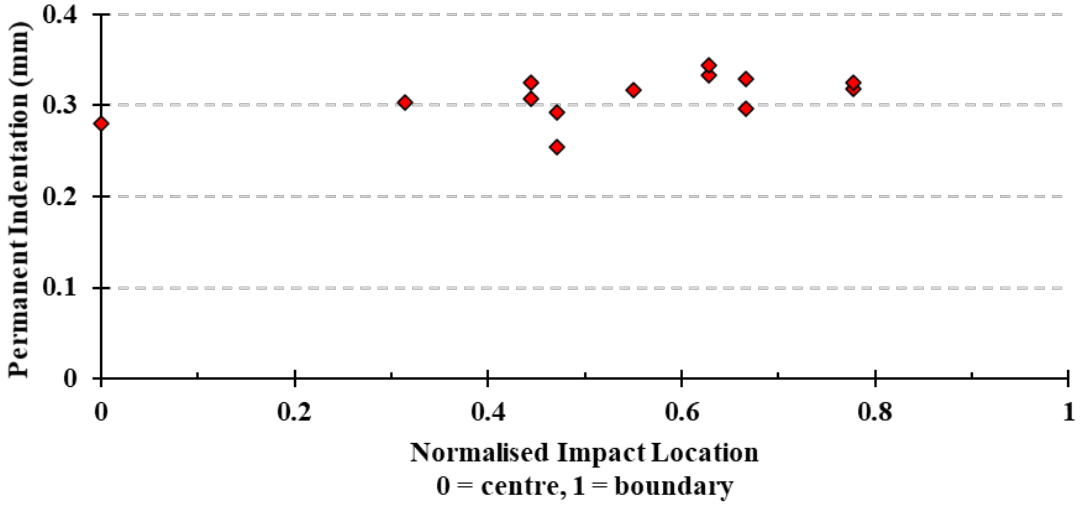


Fig. 15. Spatial variance of permanent indentation measured experimentally at different locations on the targeted panel.

5. Application of the Proposed Analytical Predictive Relationships

The application of the developed analytical model for the prediction of permanent indentation w_0 is demonstrated in this section. The considered impact scenario was a hailstone of 50.8 mm in diameter weighing 59.5 g, impacting an aluminium cladding panel with an incident velocity of 50 m/s. The targeted panel, which was fully clamped on all four edges, had dimensions of 900 mm × 900 mm × 3 mm thick, and was fabricated of alloy grade 5083-H116. The yield strength of this grade was taken as 215 MPa.

Solution:

460 The mean strain rate ($\dot{\varepsilon_m}$) which is estimated using Eq. (2) is substituted into Eq. (1) for
461 calculation of the dynamic flow stress (σ_d).

462 $$\dot{\varepsilon_m} = 2.09\left(\frac{v_0}{t}\right)^{0.45} = 2.09\left(\frac{50}{0.003}\right)^{0.45} = 166\ s^{-1}$$

463 $$\sigma_d = \sigma_y\left[1 + \left(\frac{\dot{\varepsilon_m}}{D}\right)^{\frac{1}{q}}\right] = 215\left[1 + \left(\frac{166}{6700}\right)^{\frac{1}{4}}\right] = 300\ MPa$$

464 Eq. (11a) is then made use of for predicting the amount of energy (W_p) expended in causing
465 permanent indentation. Results so obtained are then substituted into Eq. (12) for determination
466 of the maximum indentation (w_0).

467 $$w_0 = \frac{1}{2}\left(-t\frac{\mathrm{B}}{\mathrm{A}} + \sqrt{t^2\frac{\mathrm{B}^2}{\mathrm{A}^2} + \frac{4W_p}{\pi\sigma_d t\mathrm{A}}}\right)$$

468 $$= \frac{1}{2}\left(-0.003\frac{0.9422}{0.3499} + \sqrt{0.003^2\frac{0.9422^2}{0.3499^2} + \frac{4\times4.87}{\pi(300\times10^6)(0.003)(0.3499)}}\right)$$

469 $$= 0.57\ mm$$

470 The model prediction of 0.57 mm is compared against the experimental measurement of 0.59
471 mm demonstrating good consistency. Prediction-measurement comparisons across a range of
472 impact scenarios can be found in Fig. 14.

6. Conclusion

A new algebraic expression for predicting the amount of permanent indentation into the surface of an aluminium alloy panel generated by the impact of hail has been developed in this study. The strain rate effect has been incorporated to account for the hardening behaviour of the aluminium material when subject to a highly transient action of hail impact (of duration ~ 1 ms). A generalised shape function has been developed to model the unique curvature and shape of the indentation profile on the surface of the aluminium panel. The amount of energy absorbed by the plate in forming the indentation was found to consume only a tiny fraction of the (initial) kinetic energy delivered by the impact (with 6.55% and 2.09% for plate thicknesses of 3 mm and 4 mm, respectively). In impact scenarios where the amount of indentation was less than the plate thickness, radial and circumferential flexural actions consumed most of the energy, whereas contributions from membrane actions were minor. Predictions from the proposed analytical expression for the considered impact scenarios were all within 10% of the experimentally measured results. Accurate predictions of the amount of indentation can be made once the following parameters are known: size (mass) of the hail, velocity of impact, thickness and grade (yield strength) of the alloy. The outcome of the current study enables damage to cladding panels in projected hail impact scenarios to be predicted accurately without the need for any costly impact experimentations.

CRediT authorship contribution statement

Shuangmin Shi: Methodology, Investigation, Data curation, Formal analysis, Validation, Visualization, Writing – Original Draft, Writing – Review & Editing. **Nelson Lam:** Conceptualization, Writing – Review & Editing, Supervision, Funding acquisition. **Yiwen Cui:** Investigation, Data curation, Formal analysis. **Guoxing Lu:** Conceptualization, Methodology, Resources, Funding acquisition. **Emad Gad:** Conceptualization, Funding acquisition. **Lihai Zhang:** Conceptualization, Methodology, Writing – Review & Editing, Supervision, Funding acquisition, Project administration.

Declaration of competing interest

The authors declare that they have no known competing financial interests or personal relationships that could have appeared to influence the work reported in this paper.

Acknowledgements

This work is financially supported by the Australian Research Council Linkage Project (ARC LP190100208). Cash and in-kind support by Mr Ian Bennie (General Manager of *Ian Bennie and Associates*) and Mr Suresh Sutrave (Director of *Atlite Skylights*) as Partner Investigators of the linkage project are gratefully acknowledged. The authors are also grateful to Mr Kubendra Rao, Mr Jasman Anwar and Mrs Josie Stokoe for their kind help in the preparation of the test apparatus. The authors wish to thank Dr Shanqing Xu, Mrs Cong Wang and Ms Jia Ming Goh for their generous support during the experiment.

References

1. Minor, J.E., *Windborne debris and the building envelope.* Journal of Wind Engineering and Industrial Aerodynamics, 1994. **53**(1-2): p. 207-227.
2. Sparks, P., *Wind speeds in tropical cyclones and associated insurance losses.* Journal of wind engineering and industrial aerodynamics, 2003. **91**(12-15): p. 1731-1751.
3. Sparks, P.R., S. Schiff, and T. Reinhold, *Wind damage to envelopes of houses and consequent insurance losses.* Journal of wind engineering and industrial aerodynamics, 1994. **53**(1-2): p. 145-155.
4. Changnon, S.A., *Temporal and spatial distributions of damaging hail in the continental United States.* Physical Geography, 2008. **29**(4): p. 341-350.
5. Changnon, S.A., D. Changnon, and S.D. Hilberg, *Hailstorms across the nation: An atlas about hail and its damages.* ISWS Contract Report CR-2009-12, 2009.
6. Ali, M., et al., *Simple hand calculation method for estimating deflection generated by the low velocity impact of a solid object.* Australian Journal of Structural Engineering, 2014. **15**(3): p. 243-259.
7. Yang, Y., N. Lam, and L. Zhang, *Evaluation of simplified methods of estimating beam responses to impact.* International Journal of Structural Stability and Dynamics, 2012. **12**(03): p. 1250016.
8. Yang, Y., N. Lam, and L. Zhang, *Estimation of response of plate structure subject to low velocty impact by a solid object.* International journal of structural stability and dynamics, 2012. **12**(06): p. 1250053.
9. Yang, Y., et al., *Simplified analysis of low velocity impact actions on shallow domes.* International Journal of Applied Mechanics, 2013. **5**(02): p. 1350013.
10. Standard, B., *Eurocode 1: Actions on structures—.* 2010.
11. Perera, S., et al., *Deterministic solutions for contact force generated by impact of windborne debris.* International Journal of Impact Engineering, 2016. **91**: p. 126-141.
12. Sun, J., et al., *Contact forces generated by fallen debris.* Structural Engineering and Mechanics, 2014. **50**(5): p. 589-603.
13. Sun, J., et al., *Contact forces generated by hailstone impact.* International Journal of Impact Engineering, 2015. **84**: p. 145-158.
14. Sun, J., et al., *Computer simulation of contact forces generated by impact.* International Journal of Structural Stability and Dynamics, 2017. **17**(01): p. 1750005.
15. Sun, J., et al., *A note on Hunt and Crossley model with generalized visco-elastic damping.* International Journal of Impact Engineering, 2018. **121**: p. 151-156.
16. Yang, Y., et al., *An innovative procedure for estimating contact force during impact.* International Journal of Applied Mechanics, 2014. **6**(06): p. 1450079.
17. Chen, S., et al., *Experiments on an ice ball impacting onto a rigid target.* International Journal of Impact Engineering, 2022. **167**: p. 104281.
18. Shi, S., et al., *An analytical approach for modelling contact forcing function of hailstone impact.* International Journal of Solids and Structures, 2023. **269**: p. 112214.

19. Saini, D. and B. Shafei, *Prediction of extent of damage to metal roof panels under hail impact.* Engineering Structures, 2019. **187**: p. 362-371.

20. Tang, Z., et al., *Numerical and experimental investigation on hail impact on composite panels.* International Journal of Impact Engineering, 2017. **105**: p. 102-108.

21. Kim, H., D.A. Welch, and K.T. Kedward, *Experimental investigation of high velocity ice impacts on woven carbon/epoxy composite panels.* Composites Part A: applied science and manufacturing, 2003. **34**(1): p. 25-41.

22. Park, H. and H. Kim, *Damage resistance of single lap adhesive composite joints by transverse ice impact.* International Journal of Impact Engineering, 2010. **37**(2): p. 177-184.

23. Wu, X., et al., *Dynamic responses and energy absorption of sandwich panel with aluminium honeycomb core under ice wedge impact.* International Journal of Impact Engineering, 2022. **162**: p. 104137.

24. Rhymer, J., H. Kim, and D. Roach, *The damage resistance of quasi-isotropic carbon/epoxy composite tape laminates impacted by high velocity ice.* Composites Part A: Applied Science and Manufacturing, 2012. **43**(7): p. 1134-1144.

25. Cai, W., L. Zhu, and X. Qian, *Dynamic responses of steel plates under repeated ice impacts.* International Journal of Impact Engineering, 2022. **162**: p. 104129.

26. Cai, W., et al., *Numerical simulations for plates under ice impact based on a concrete constitutive ice model.* International journal of impact engineering, 2020. **143**: p. 103594.

27. Herbin, A. and M. Barbato, *Fragility curves for building envelope components subject to windborne debris impact.* Journal of Wind Engineering and Industrial Aerodynamics, 2012. **107**: p. 285-298.

28. Alphonso, T. and M. Barbato, *Experimental fragility curves for aluminum storm panels subject to windborne debris impact.* Journal of Wind Engineering and Industrial Aerodynamics, 2014. **134**: p. 44-55.

29. Chen, W., H. Hao, and H. Du, *Failure analysis of corrugated panel subjected to windborne debris impacts.* Engineering Failure Analysis, 2014. **44**: p. 229-249.

30. Carney, K.S., et al., *A phenomenological high strain rate model with failure for ice.* International Journal of Solids and Structures, 2006. **43**(25-26): p. 7820-7839.

31. Tippmann, J.D., H. Kim, and J.D. Rhymer, *Experimentally validated strain rate dependent material model for spherical ice impact simulation.* International journal of impact engineering, 2013. **57**: p. 43-54.

32. Pernas-Sánchez, J., et al., *Numerical modeling of ice behavior under high velocity impacts.* International Journal of Solids and Structures, 2012. **49**(14): p. 1919-1927.

33. Liu, K., P. Li, and Z. Wang, *A rate-sensitive and pressure-dependent failure criterion for hail ice.* International Journal of Impact Engineering, 2022. **168**: p. 104291.

34. Cui, Q. and J. Yang, *Evaluation of numerical simulation methods and ice material models for intermediate-velocity hail impact simulation.* Engineering Structures, 2021. **244**: p. 112831.

35. Jones, N., *A theoretical study of the dynamic plastic behavior of beams and plates with finite-deflections.* International Journal of Solids and Structures, 1971. **7**(8): p. 1007-1029.

36. Jones, N., *On the mass impact loading of ductile plates.* Defence Science Journal, 2003. **53**(1): p. 15.

37. Jones, N., S.-B. Kim, and Q. Li, *Response and failure of ductile circular plates struck by a mass.* 1997.

38. Lu, G. and T. Yu, *Energy absorption of structures and materials*. 2003: Elsevier.

39. Jones, N., *Impact loading of ductile rectangular plates.* Thin-walled structures, 2012. **50**(1): p. 68-75.

40. Duffey, T.A., *Large deflection dynamic response of clamped circular plates subjected to explosive loading*. 1967, Sandia Corp., Albuquerque, N. Mex.

41. Calder, C.A. and W. Goldsmith, *Plastic deformation and perforation of thin plates resulting from projectile impact.* International Journal of Solids and Structures, 1971. **7**(7): p. 863-881.

42. Mohotti, D., et al., *Out-of-plane impact resistance of aluminium plates subjected to low velocity impacts.* Materials & Design, 2013. **50**: p. 413-426.

43. Pathirana, M., et al., *Damage modelling of aluminium panels impacted by windborne debris.* Journal of Wind Engineering and Industrial Aerodynamics, 2017. **165**: p. 1-12.

44. Shi, S., et al., *Indentation into an aluminium panel by the impact of a rigid spherical object.* Thin-Walled Structures, 2022. **180**: p. 109935.

45. Liu, B., R. Villavicencio, and C.G. Soares, *On the failure criterion of aluminum and steel plates subjected to low-velocity impact by a spherical indenter.* International Journal of Mechanical Sciences, 2014. **80**: p. 1-15.

46. Bennie, I., *Advice sought from personal communication in 2021 with Ian Bennie of Ian Bennie & Associates which is the National Association of Testing Authorities (NATA) sole accredited testing laboratory in Australia*. 2021.

47. Gharababaei, H. and A. Darvizeh, *Experimental and Analytical Investigation of Large Deformation of Thin Circular Plates Subjected to Localized and Uniform Impulsive Loading#.* Mechanics based design of structures and machines, 2010. **38**(2): p. 171-189.

48. Jones, N., *Structural impact*. 2011: Cambridge university press.

49. Li, D., et al., *Energy absorption of aluminum panels subjected to gelatin projectile impact.* Latin American Journal of Solids and Structures, 2019. **16**.

50. Zaera, R., A. Arias, and C. Navarro, *Analytical modelling of metallic circular plates subjected to impulsive loads.* International journal of solids and structures, 2002. **39**(3): p. 659-672.

51. Shah, Q.H. and Y.A. Abakr, *Effect of distance from the support on the penetration mechanism of clamped circular polycarbonate armor plates.* International Journal of Impact Engineering, 2008. **35**(11): p. 1244-1250.